



Flexible Micro-Supercapacitors with Enhanced Energy Density Utilizing Flash Lamp Annealed Graphene-Carbon Nanotube Composite Electrodes

Yusik Myung^[a] and TaeYoung Kim^{*[a, b]}

As demand for micro-power sources grows, micro-supercapacitors (MSCs) have become critical for miniaturized devices, offering robust electrochemical energy storage. However, the challenge remains to develop a simple, scalable fabrication method that achieves both high energy and power densities. In this study, we present a refined approach to fabricating MSCs with 3D interconnected graphene/carbon nanotube (CNT) composite electrodes. Our method combines flash lamp annealing (FLA) and laser ablation, where FLA converts graphene oxide (GO) and CNT composite films into 3D-structured graphene/CNT electrodes, and laser ablation precisely patterns them into interdigitated designs. This dual-process technique produces MSCs with exceptional electro-

chemical performance, including an impressive areal capacitance of 26.11 mF/cm^2 and a volumetric capacitance of 31.88 F/cm^3 . These devices also achieve energy densities of $3.72 \mu\text{Wh}/\text{cm}^2$ and $4.43 \text{ mWh}/\text{cm}^3$, maintaining 97% of their initial capacitance under extreme bending, demonstrating outstanding mechanical flexibility and durability. Furthermore, the scalability of this method was validated by configuring MSCs in series and parallel, achieving enhanced voltage and current outputs without additional interconnections. Overall, the integration of FLA and laser ablation holds significant promise for advancing the performance and scalability of micro-sized energy storage devices, addressing the growing need for efficient, flexible, and high-capacity micro-power sources.

Introduction

The rapid advancement of portable electronics, such as wearable and miniaturized devices, has driven an urgent need for energy storage solutions that are efficient, compact, lightweight, and flexible.^[1–3] Although micro-batteries are the dominant power sources for these applications, their limited lifespan (ranging from 500 to 10,000 cycles) and low power density pose significant challenges, making frequent replacements or costly maintenance necessary.^[2] Micro-fuel cells, while an alternative, suffer from slow oxygen reduction reactions (ORRs) kinetics and the requirement for a continuous hydrogen supply, which limits their practicality in microchips and other small-scale devices.^[4] In this context, micro-supercapacitors (MSCs) have emerged as a highly promising alternative due to their superior power density, rapid charge-discharge capability, and long cycle life. MSCs store energy through either capacitive ion adsorption-desorption or pseudo-capacitive Faradaic reactions at the electrode-electrolyte interface,^[2,5] allowing them to achieve lifetimes of over 100,000 cycles and power densities that exceed those of micro-batteries by an order of magnitude.

Efforts in recent research have been directed toward integrating MSCs into chips or flexible substrates to serve as energy storage solutions for embedded microsystems.^[1,6] MSCs typically employ planar interdigitated electrode configuration, which offer distinct advantages over the conventional stacked designs. These include more efficient use of electrode materials, shorter ion diffusion paths, greater mechanical flexibility, and scalability for large-scale production.^[7,8] Such planar MSC have the potential to be seamlessly integrated into wireless devices or microchips, offering an efficient means of storing and delivering electric energy.^[9]

A wide range of materials, including carbon-based materials, transition metal oxides, and conductive polymers, have been explored for MSC electrodes.^[10–12] Transition metal oxides and conductive polymers exhibit high specific capacities through Faradaic redox reactions, but their practical applications are limited by poor rate performance and limited cycle stability.^[13,14] In contrast, carbon-based materials, which store charge via non-Faradaic processes, offer excellent rate capability, cycle stability, and moderate specific capacities. Among these, graphene, a two-dimensional carbon sheet, has garnered particular attention as an MSC electrode material due to its exceptional properties. These include a high theoretical specific surface area ($\sim 2,630 \text{ m}^2/\text{g}$), excellent electrical conductivity ($\sim 10^8 \text{ S/m}$), and high theoretical specific capacitance ($\sim 550 \text{ F/g}$).^[7,15–18] Reduced graphene oxide (rGO), obtained by the chemical or thermal reduction of graphene oxide (GO), has been extensively studied as an electrode material in supercapacitors. However, traditional reduction methods often involve toxic chemicals, are energy-intensive, and are not well-suited for scalable device fabrication. Consequently, there is a growing demand for the development

[a] Y. Myung, T. Kim

Department of Materials Science and Engineering, Gachon University, 1342 Seongnam-daero, Sujeong-gu Seongnam-si, Gyeonggi-do 13120, Republic of Korea
E-mail: taeykim@gachon.ac.kr

[b] T. Kim

R&D Center, ENCATE, #1009 SICOX Tower, 484 Dunchon-daero, Jungwon-gu, Seongnam-si, Gyeonggi-do 13229, Republic of Korea

Supporting information for this article is available on the WWW under <https://doi.org/10.1002/batt.202400557>

of simple, rapid, energy-efficient, and low-cost techniques to fabricate graphene-based MSCs, particularly on flexible substrates without using toxic chemicals or high temperature processes.

Various methods have been employed to fabricate graphene-based microelectrodes for MSCs, including lithographic microfabrication,^[19,20] inkjet printing,^[21–23] screen printing,^[24,25] laser processing,^[3,26–30] and photochemical reduction.^[18] Lithographic microfabrication, which combines photolithography with wet or dry etching, can produce high-resolution graphene microelectrode patterns.^[19,20] However, this technique involves multiple complex steps, such as spin coating, mask exposure,^[31] etching,^[32] and the chemical or thermal reduction of GO,^[15, 33] making it time-consuming and unsuitable for mass production. On the other hand, direct printing techniques such as inkjet and screen printing offer a more cost-effective route for creating graphene micropatterns on flexible substrate,^[22,23] but these methods require graphene-formulated inks or pastes typically containing polymeric binders or surfactants, which reduce the electrical conductivity and porosity of the resulting electrodes, leading to lower performance.^[34] Photochemical reduction of GO,^[35, 36] though offering precise control and high efficiency, requires pre-patterned masks and lengthy processing times under UV light, limiting its practical applicability.^[18] Laser-based techniques, including pyrolysis,^[37–39] reduction,^[40–42] sintering,^[27,43] and ablation,^[29] simplify the fabrication processes for graphene-based MSCs but generally result in low areal capacitance, which constrains their energy storage capacity.

In contrast, flash lamp annealing (FLA) has emerged as a highly promising technique for rapidly fabricating large-scale graphene microelectrodes on flexible substrates. FLA utilizes intense pulsed light from xenon (Xe) flash lamps, which deliver rapid heating to thin film within microseconds to milliseconds. This enables high-speed processing of thin materials without damaging underlying low-temperature substrates such as polymers and paper. Additionally, FLA is scalable and compatible with roll-to-roll processing, making it ideal for large-area manufacturing.^[36,44] Previous studies have demonstrated the potential of FLA for the photothermal reduction of GO films,^[45] and our prior work successfully employed FLA to create interdigitated graphene microelectrodes, which were further functionalized with Co–Mn layered double hydroxide to fabricate hybrid MSCs.^[46] Despite these advancements, current methods often fall short of achieving high areal and volumetric energy and power densities required for advanced applications.

In this study, we present a significant advancement by integrating FLA with laser ablation to fabricate interdigitated microelectrodes composed of graphene and carbon nanotubes (CNTs) on flexible substrates. This combination enables rapid, scalable production of high-performance in-plane MSCs. The graphene/CNT microelectrodes processed via FLA and laser ablation exhibit outstanding electrochemical performance, with a high areal capacitance of 26.11 mF/cm², an areal energy density of 3.72 µWh/cm², and an areal power density of 11.73 mW/cm². These metrics surpass those of previously reported carbon-based MSCs. The results demonstrate the

effectiveness of combining FLA and laser ablation for fabricating flexible, high-performance MSCs, significantly improving both energy and power densities.

Results and Discussion

Figure 1 presents a schematic illustration of the fabrication process for interdigitated graphene/CNT microelectrodes on a flexible substrate, employing flash lamp annealing (FLA) and laser ablation techniques.

The process starts with the preparation of a thin film of GO and CNT (GO/CNT) composites. This is achieved by blade-coating an aqueous dispersion of GO and CNT in a specified ratio onto a flexible substrate, such as poly(ethylene terephthalate) (PET). In the subsequent step, the GO/CNT composites film undergoes FLA. During this stage, the film is exposed to high-intensity light pulses emitted from a Xe flash lamp, which rapidly heats the GO/CNT film to temperatures exceeding 1,000 K in under 100 milliseconds. This rapid thermal processing efficiently reduces the GO to photothermally reduced graphene oxide (referred to as FLAG). The intense light pulses not only induce a reduction of GO but also lead to a partial restructuring of the composite, resulting in a more interconnected and porous network. This corrugated network of carbons and open pore structure is beneficial for electrochemical performance, as it provides improved pathways for ion diffusion and electron transport, thus boosting charge storage and delivery efficiency. After the FLA-based photothermal reduction, a thin layer of gold is deposited onto the surface of FLAG/CNT film, serving as current collectors. This gold layer ensures efficient electrical conductivity and enhances the overall performance of the microelectrodes. The final step in the fabrication process involves laser ablation to pattern the FLAG/CNT film into precise, comb-like interdigitated electrodes. Laser ablation is a crucial step, enabling the formation of well-defined, high-resolution electrode patterns necessary for optimal charge storage and delivery in MSCs.

The resulting microelectrodes, referred to as LA-FLAG/CNT, benefit from the precise and flexible nature of the laser ablation process. This technique allows for the creation of various electrode geometries and sizes, tailored to specific application requirements. Additionally, the combination of FLA and laser ablation proves to be cost-effective and scalable compared to conventional MSC fabrication methods. The FLA process enables the rapid processing of large areas of FLAG/CNT film in just tens of milliseconds, significantly reducing fabrication time and energy consumption. Moreover, the laser ablation technique offers precise control over electrode design, enabling the customization of microelectrode patterns for specific needs, enhancing adaptability of this approach for diverse energy storage applications.

The FLA-based photothermal reduction of GO/CNT composites to FLAG/CNT leads to notable structural and morphological changes in the GO material, confirmed by comprehensive analysis. X-ray diffraction (XRD) patterns (Figure 2a) reveal transformation of the graphitic structure during this process.

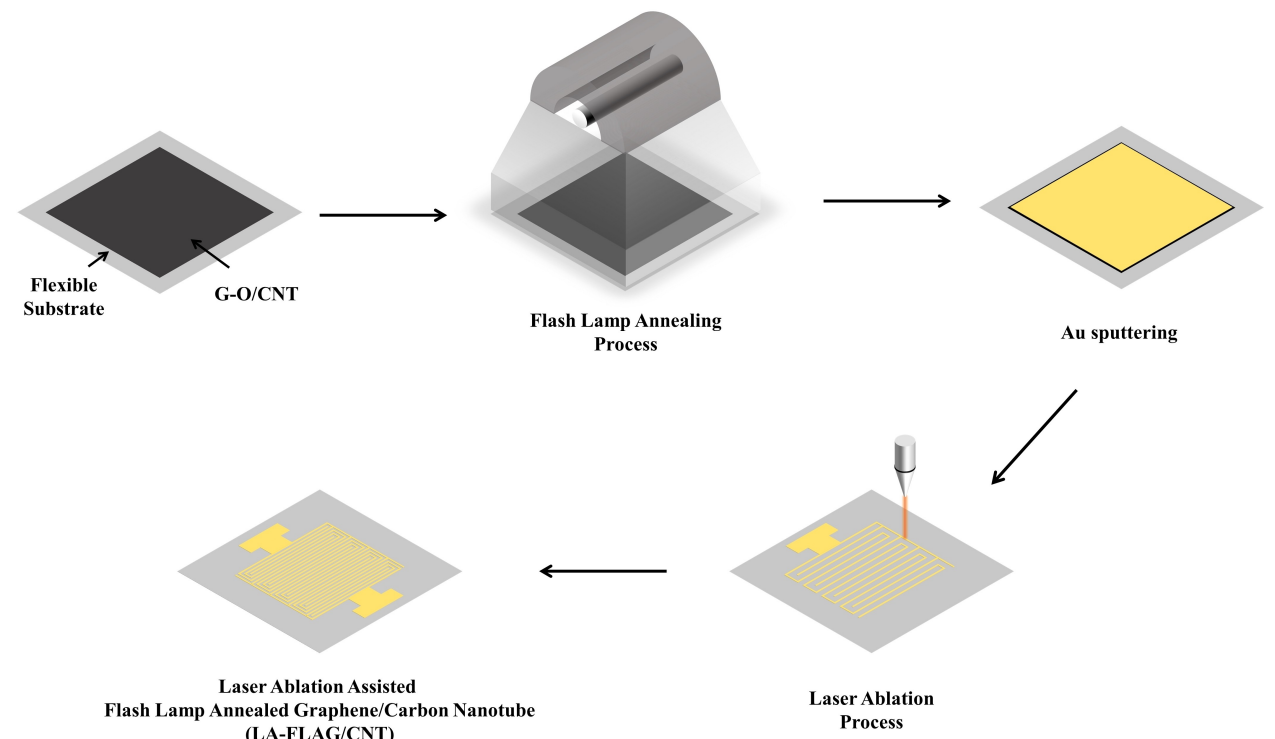


Figure 1. Schematic illustration of the laser ablation-assisted flash lamp annealing (LA-FLAG) process for fabricating graphene/carbon nanotube microelectrodes.

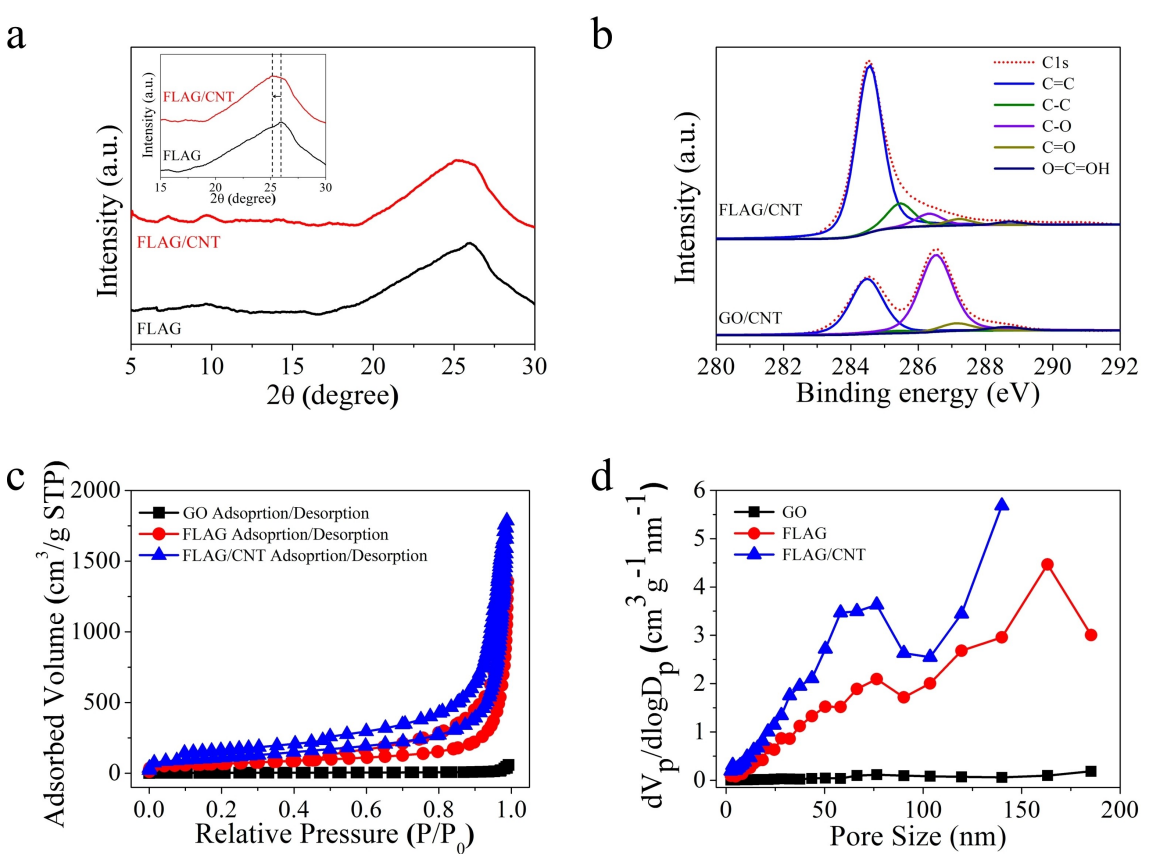


Figure 2. Characterization of FLAG/CNT composite. (a) XRD patterns of FLAG and FLAG/CNT. (b) C1s XPS spectra of FLAG/CNT and GO/CNT film. (c) BET isotherms of GO, FLAG, and FLAG/CNT, (d) BJH pore size distribution of GO, FLAG, and FLAG/CNT.

Initially, GO exhibited a distinct peak at $2\theta = 11.2^\circ$, corresponding to an interlayer spacing (d_{001}) of 0.789 nm. For the GO/CNT composite, the peak shifted to $2\theta = 9.19^\circ$ with an increased interlayer spacing ($d_{001} = 0.961$ nm), indicating CNT intercalation between GO layers (Figure S1). After FLA, this peak disappeared, and a new peak emerged at $2\theta = 25.9^\circ$, corresponding to a d_{002} spacing of 0.343 nm for FLAG. Interestingly, FLAG/CNT showed a slight shift in the peak to $2\theta = 25.4^\circ$, reflecting an increase in interlayer spacing from 0.343 nm to 0.350 nm. This expanded spacing is crucial for enhancing electrochemical performance, as it allows for better ion adsorption on the electrode surface, contributing to improved capacitance. X-ray photoelectron spectroscopy (XPS) provided further confirmation of the structural transformation, showing a substantial increase in the C/O ratio from 1.94 before FLA to 24.1 after the process, indicating effective removal of oxygen-containing functional groups and the successful reduction of GO to FLAG (Figure 2b). The specific surface area and porous structure of FLAG/CNT were characterized using N_2 adsorption-desorption analysis (Figure 2c-d). FLAG/CNT exhibited a significantly larger specific surface area (397.47 m²/g) compared to FLAG (236.94 m²/g), along with a slight increase in pore diameter (~34 nm for FLAG/CNT vs. ~27 nm for FLAG), as shown in Table S1. These properties are beneficial for enhancing the electrochemical performance of the electrodes by improving ion transport and charge storage capacity. Raman spectroscopy further corroborated these findings (Figure S2). GO exhibited two prominent peaks at ~ 1350 cm⁻¹ and ~ 1591 cm⁻¹, corresponding to the D and G bands, respectively, with an intensity ratio (I_D/I_G) of 1.022. After FLA, the G band shifted closer to that of pristine graphite (~ 1575 cm⁻¹), appearing at 1585 cm⁻¹ and 1583 cm⁻¹, respectively.^[46] The I_D/I_G ratio for LA-FLAG/CNT was significantly lower (0.11) compared to that of LA-FLAG (1.08),

suggesting a more effective photothermal reduction of GO in the presence of CNTs. Additionally, the strong 2D band at ~ 2700 cm⁻¹ for both LA-FLAG and LA-FLAG/CNT indicated the restoration of graphitic electronic conjugation following the reduction of GO.^[47]

These structural and morphological analyses demonstrate the effectiveness of FLA in not only reducing GO to graphene but also enhancing key electrochemical properties of the FLAG/CNT composites. The increase in interlayer spacing, larger specific surface area, improved pore structure, and restoration of electronic properties make FLAG/CNT composites highly promising for high-performance MSCs. These features directly contribute to superior energy and power densities, making them suitable for advanced energy storage applications.

Figure 3a shows a photograph of the as-prepared interdigitated LA-FLAG/CNT microelectrodes with varying interspace patterns.

Optical microscope images (Figure 3b) illustrate the clear, well-defined boundaries between the LA-FLAG/CNT microelectrodes, demonstrating the precision of the laser ablation process. A cross-sectional SEM image (Figure 3c) highlights the morphological changes induced by the FLA process. The region exposed to the light pulses becomes highly porous, with the LA-FLAG/CNT film moderately expanding to an average thickness of ~ 8.19 μ m. In contrast, LA-FLAG alone expands significantly more, reaching a thickness exceeding 100 μ m. The lower thickness of LA-FLAG/CNT electrodes suggests a denser structure per unit area, which can lead to higher areal and volumetric capacitance. A side view SEM image of the LA-FLAG/CNT electrodes on the substrate reveals the expansion of the electrode after the FLA process. High-resolution SEM images further demonstrate interconnected 3D graphene sheets and a reticular network of CNTs forming around the 3D graphene

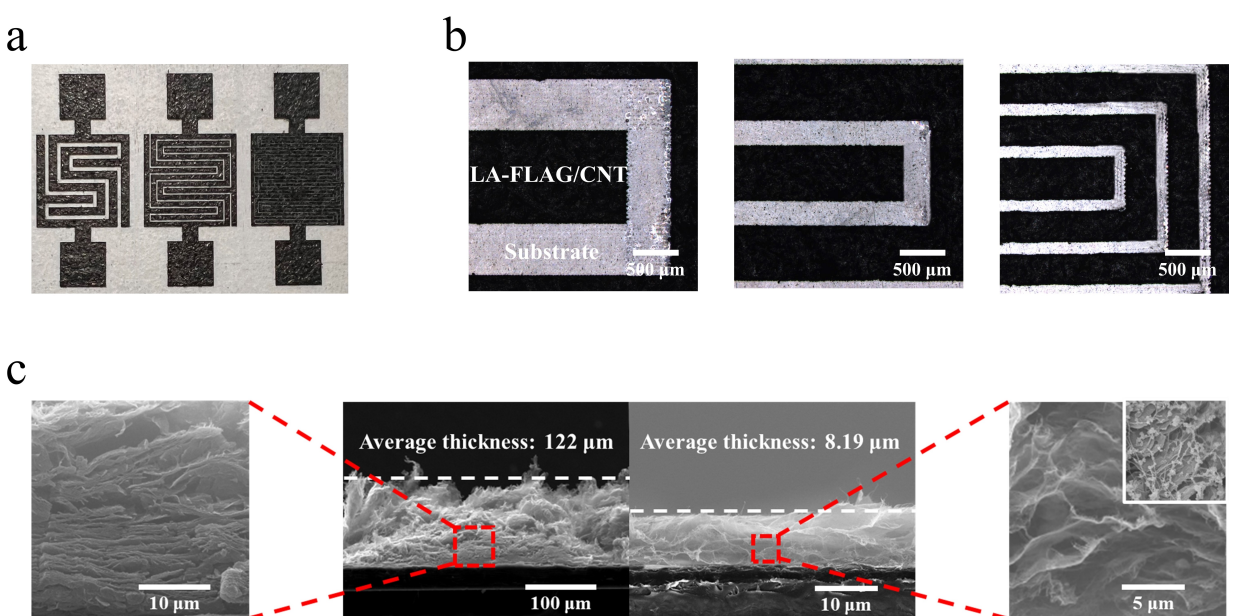


Figure 3. Characterization of LA-FLAG/CNT micro-electrodes. (a) Digital image of LA-FLAG micro-electrodes. (b) Optical microscope images showing the precise patterning of LA-FLAG/CNT electrodes. (c) Cross-sectional SEM images comparing the morphology of LA-FLAG electrodes and LA-FLAG/CNT electrodes.

structure, resulting in a highly accessible surface area with excellent electrical conductivity. When comparing high-magnification SEM images of LA-FLAG and LA-FLAG/CNT electrodes, the LA-FLAG electrode exhibits densely stacked graphene sheets at the bottom, reducing ion accessibility. In contrast, LA-FLAG/CNT electrodes form an interconnected 3D network, greatly enhancing surface accessibility for ion transport and charge storage, which improves the electrochemical performance of the MSCs. These observations confirm that the combination of FLA and laser ablation techniques not only achieves precise patterning but also optimizes the structural and morphological properties of the electrodes. The dense, highly accessible network in LA-FLAG/CNT electrodes is particularly advantageous for applications requiring high areal and volumetric capacitance, making them ideal for advanced micro-supercapacitors.

We fabricated MSCs using LA-FLAG/CNT microelectrodes paired with a polymer gel electrolyte of $\text{H}_2\text{SO}_4/\text{PVA}$ and evaluated their electrochemical performance. First, we optimized the ratio between FLAG and CNT in the FLAG/CNT electrodes. Among the various ratios tested, the highest areal capacitance of $\sim 16 \text{ F/cm}^2$ was achieved with a GO/CNT ratio of 1:1 (Figure S3). This ratio was subsequently used for fabricating the LA-FLAG/CNT microelectrodes. Next, we optimized the dimensions of the LA-FLAG/CNT microelectrodes by varying the width, interspace, and length of the interdigitated electrodes. The electrochemical performance of microelectrodes with different designs was evaluated through cyclic voltammetry (CV) at a scan rate of 100 mV/s (Figure S4). Increasing the number of interdigitated patterns while decreasing the interspace significantly enhanced areal and volumetric capacitance. A smaller interspace reduces the diffusion path of electrolyte

ions, facilitating faster ion transport and boosting capacitance. In interdigitated structures, capacitance is proportional to the ratio of electrode width (w) to interspace (i).^[47] The laser ablation techniques simplified the adjustment of both the width and interspace of the microelectrodes, optimizing ion transport and enhancing capacitance.^[48]

Comparative electrochemical performance of MSCs fabricated with LA-FLAG/CNT and LA-FLAG microelectrodes was evaluated through CV at a scan rate of 100 mV/s (Figure 4a). The LA-FLAG/CNT MSCs exhibited nearly rectangular CV profiles, which were significantly larger than those of LA-FLAG MSCs, indicating enhanced capacitance. The superior performance of LA-FLAG/CNT electrodes is attributed to the uniformly created open pore structure throughout the electrodes, in contrast to the dense stacking of graphene layers in the lower part of the LA-FLAG electrode. In the LA-FLAG electrode, the FLA process unevenly reduces GO, leading to uneven expansion of the graphene layers, which results in densely stacked sheets that are less accessible to electrolyte ions (Figure 3c). However, in the LA-FLAG/CNT electrodes, the CNTs act as effective photon energy conduits during FLA, efficiently delivering photon energy to GO and facilitating uniform photothermal reduction. Additionally, CNTs serve as structural pillars, preventing graphene layer stacking (as illustrated in Figure S5), thus enhancing electrolyte ion accessibility and improving the overall capacitance of the MSCs. This combination of features enables LA-FLAG/CNT electrodes to outperform LA-FLAG in terms of energy and power density, making them highly suitable for advanced micro-supercapacitor applications.

The CV experiments at various scan rates confirmed that LA-FLAG/CNT MSCs maintained a rectangular shape even at a scan rate of 1 V/s (Figure 4b and Figure S6), indicating excellent rate

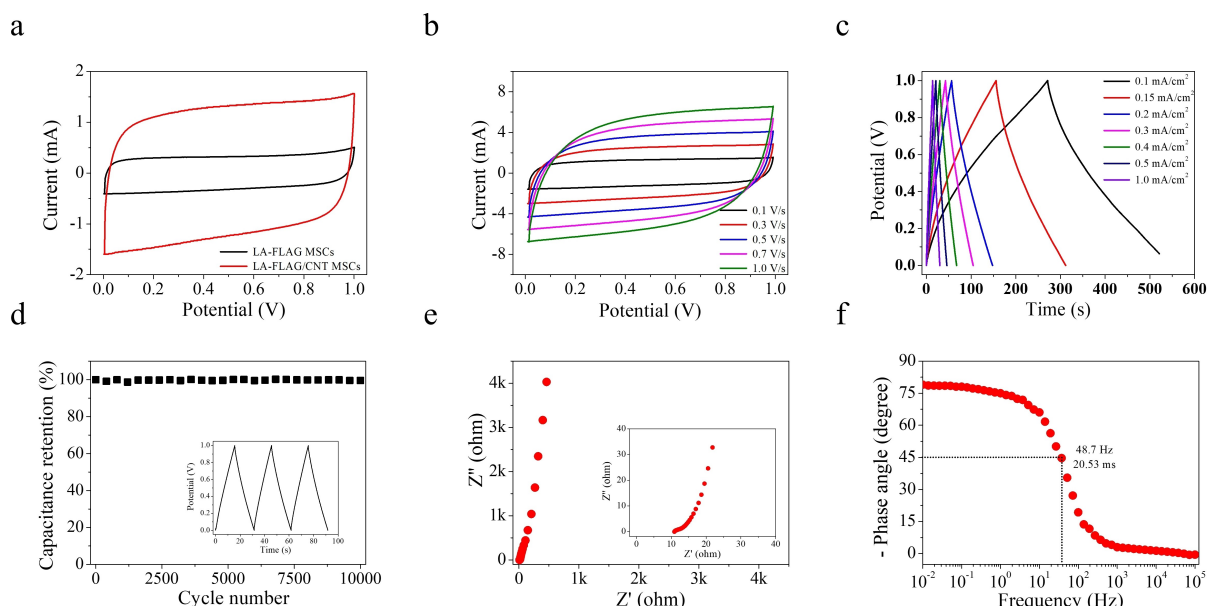


Figure 4. Electrochemical characterization of LA-FLAG/CNT MSCs. (a) CV curves of LA-FLAG MSCs and LA-FLAG/CNT MSCs. (b) CV curve of LA-FLAG/CNT MSCs at various scan rates from 0.1 to 1.0 V/s. (c) Galvanostatic charge-discharge (GCD) curves of LA-FLAG/CNT MSCs at different current densities. (d) Cycling stability of LA-FLAG/CNT MSCs over 10,000 cycles. Inset: GCD curves at a current density of 1.0 mA/cm². (e) Nyquist plots of LA-FLAG/CNT MSCs with an inset showing the high-frequency region. (f) impedance phase angle as a function of frequency for LA-FLAG/CNT MSCs.

capability. The galvanostatic charge-discharge (GCD) profiles at current densities ranging from 0.1 to 10 mA/cm² (Figure 4c and Figure S6) further highlighted the superior performance of LA-FLAG/CNT MSCs. At 0.1 mA/cm², the areal capacitance reached 26.11 mF/cm², and the volumetric capacitance was 31.88 F/cm³. Even at a higher current density of 1.0 mA/cm², the values were still significant, with an areal capacitance of 13.02 mF/cm² and volumetric capacitance of 15.89 F/cm³. These values far surpass those reported for other carbon-based MSCs, including laser-written GO film (0.51 mF/cm² and 3.1 F/cm³),^[49] laser-scribed graphene (LSG) (2.32 mF/cm² and 3.05 F/cm³),^[26] graphene/CNT composites (2.16 mF/cm² and 1.08 F/cm³),^[50] layer-by-layer printed graphene (38.4 F/cm³),^[51] exfoliated graphene (5.4 mF/cm² and 27 F/cm³),^[34] CO₂ laser scribed graphene (25.1 mF/cm² and 6.27 F/cm³),^[3] laser induced porous carbon fiber (1.57 mF/cm² and 3.14 F/cm³),^[52] N-doped porous carbon aerogel graphene (NP_{CA}) (25.6 mF/cm²),^[53] and CNT (25.3 F/cm³).^[54] The LA-FLAG/CNT MSCs demonstrated exceptional rate capability and cyclability. After 10,000 cycles, the devices retained ~99.5% of their initial capacitance (Figure 4d), highlighting their excellent cycling stability. Electrochemical impedance spectroscopy (EIS) analysis confirmed efficient ion transport within the LA-FLAG/CNT MSCs. The device exhibited pure capacitive behavior even at high frequencies, with a small equivalent series resistance (ESR) of 10.8 Ω in the high-frequency region (Figure 4e). This low ESR reflects reduced internal resistance in the electrode and minimized contact resistance between the device and the external circuit.^[55] The phase angle dependence on frequency for LA-FLAG/CNT is shown in Figure 4f. The characteristic frequency, f_0 , at a phase angle of -45° was ~48.7 Hz for LA-FLAG/CNT MSCs, compared to ~16 Hz for LA-FLAG MSCs (Figure S7). The corresponding time constant ($\tau_0 = 1/f_0$) was calculated to be 20.53 ms, significantly lower than that of commercial activated carbon-based supercapacitor (10,000 ms) and comparable to aluminum electrolytic capacitor (1 ms) (Table S3). This time constant is much lower than those of previously reported supercapacitors using activated carbon (700 ms),^[56] vertically aligned graphene (250–290 ms),^[57,58]

vertically aligned carbon nanotubes (21 ms),^[59] and planar MSCs based on onion-like carbon (26 ms).^[56]

The mechanical robustness of the LA-FLAG/CNT MSCs was assessed by conducting CV experiments under different bending angles, from 0 to 180° (Figure 5a). Remarkably, the CV curve shapes remained almost unchanged across all bending angles, with the device retaining approximately 97% of the initial capacitance measured in the flat state (0°) even when bent at 180° (Figure 5b). This outstanding mechanical flexibility shows that LA-FLAG/CNT MSCs maintain excellent electrochemical performance without delamination of the microelectrodes, even under random bending conditions.

Given that single MSCs typically offer limited energy storage capacity, practical applications often require interconnecting multiple MSCs in series or parallel configurations to enhance their performance. The adaptability of LA-FLAG/CNT MSCs for such configurations was demonstrated by interconnecting several devices in both series and parallel arrangements (Figure 6).

A key advantage of LA-FLAG/CNT MSCs is that they can be directly connected without the need for additional processes, such as metal-based interconnection or contacts. This simplifies the design and increases the efficiency of the overall system. The interdigitated LA-FLAG/CNT MSCs exhibited excellent control over operating voltage and capacitance (Figure 6a–d), confirming the versatility of these devices in tunable energy storage setups. In a tandem configuration, LA-FLAG/CNT MSCs connected in 2-series and 2-parallel arrangements exhibited simultaneous improvements in both voltage and current output (Figure 6e, f). This result demonstrates the scalability of LA-FLAG/CNT MSCs, meeting the demands for micro-sized energy storage devices that operate with high currents and voltages over short time intervals.^[60,61]

High energy and power densities are essential for the effective performance of wearable and flexible electronics.^[62,63] Our LA-FLAG/CNT MSCs exhibited superior energy and power densities compared to other MSCs reported in the literature. As shown in the Ragone plot (Figure 7), achieved an areal energy

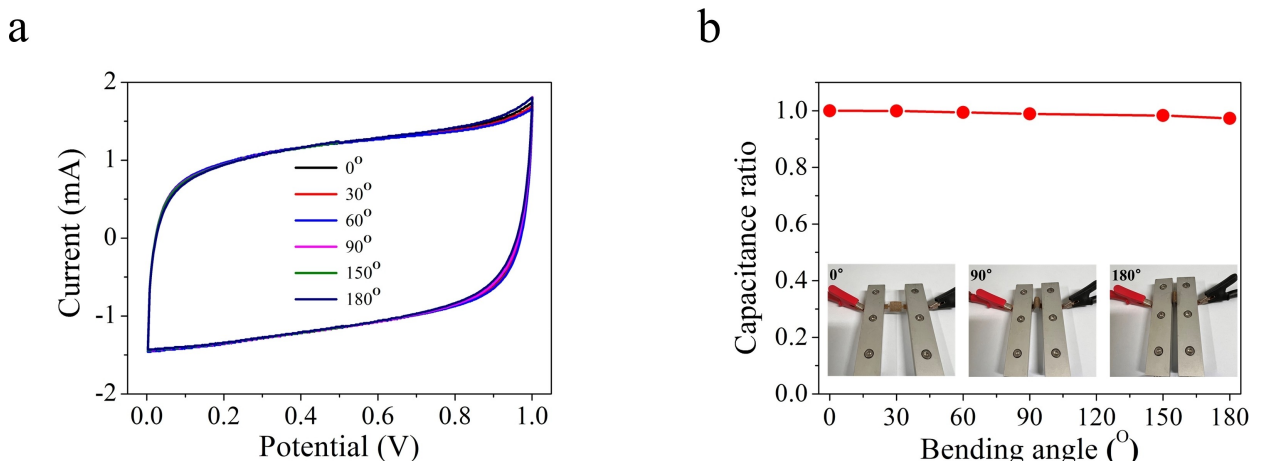


Figure 5. Flexibility of LA-FLAG/CNT MSCs. (a) CV curves of LA-FLAG/CNT MSCs at different bending angles, measured at a scan rate of 100 mV/s. (b) Capacitances of LA-FLAG/CNT MSCs as a function of bending angles. Inset: optical images showing LA-FLAG/CNT MSCs tested at various bending angles.

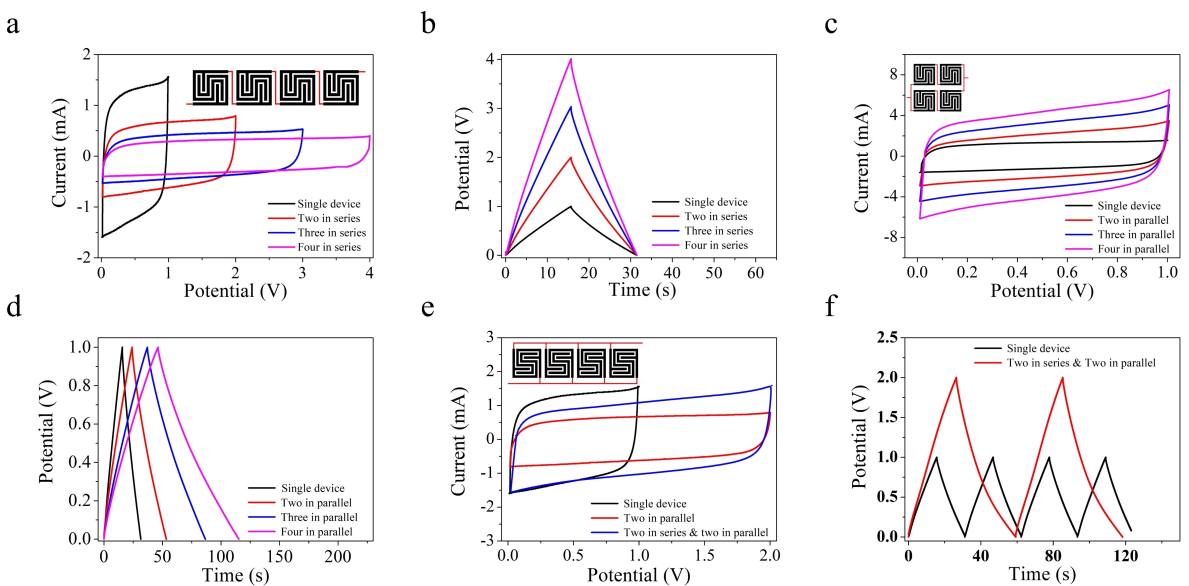


Figure 6. Integration of LA-FLAG/CNT MSCs. (a) CV curves of four MSCs connected in series at scan rate of 100 mV/s. (b) GCD curves of four MSCs connected in series at a current density of 1.00 A/cm². (c) CV curves of four MSCs connected in parallel at a scan rate of 100 mV/s. (d) GCD curves of four MSCs connected in parallel at a current density of 1.00 A/cm². (e, f) CV and GCD curves of MSCs connected in a 2-series and 2-parallel configuration at 100 mV/s and 1.00 A/cm², respectively.

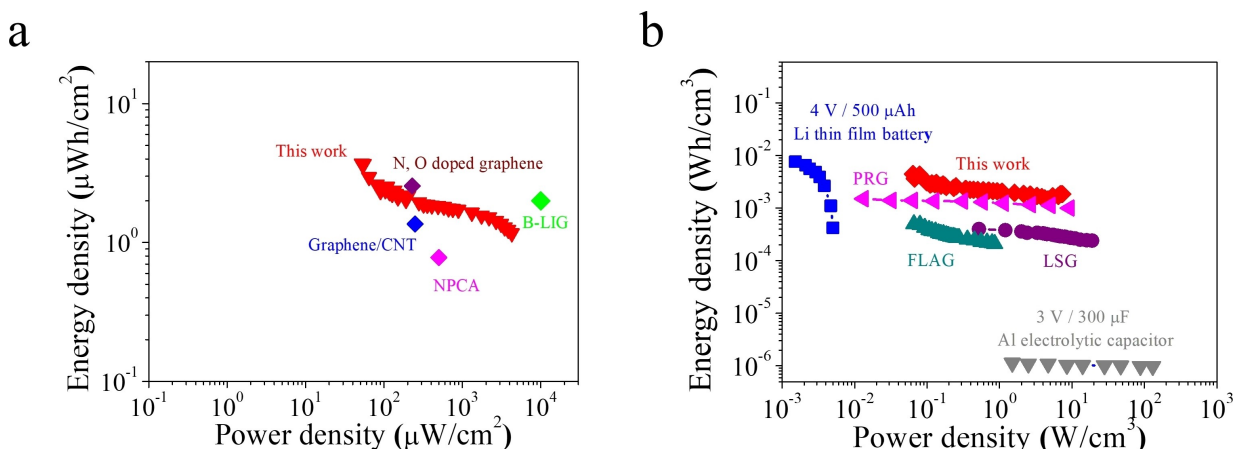


Figure 7. Ragone plot of LA-FLAG/CNT MSCs and other graphene-based MSCs. (a) Areal-based Ragone plot. (b) Volumetric-based Ragone plot

density of 3.72 $\mu\text{Wh}/\text{cm}^2$, which outperformed other MSCs, such as boron-doped laser-induced graphene (B-LIG) (2 $\mu\text{Wh}/\text{cm}^2$),^[27] N-doped porous carbon aerogel graphene (NPCA) (0.78 $\mu\text{Wh}/\text{cm}^2$),^[53] graphene/CNT composites (1.36 $\mu\text{Wh}/\text{cm}^2$),^[64] and nitrogen/oxygen-doped graphene ink (N,O-doped graphene) (2.56 $\mu\text{Wh}/\text{cm}^2$).^[65]

In terms of volumetric energy density, the LA-FLAG/CNT MSCs achieved a maximum of 4.43 mWh/cm³, which is significantly higher than most reported carbon-based MSCs. For comparison, this surpasses laser-written GO film (0.43 mWh/cm³),^[49] laser-scribed graphene (LSG) (~0.4 mWh/cm³),^[26] layer-by-layer printed graphene (7 mWh/cm³),^[51] graphene/ethyl cellulose composites (1.29 mWh/cm³),^[66] photochemically reduced graphene (PRG) (1.5 mWh/cm³),^[18] ~1.88 mWh/cm³ for laser-irradiated graphene,^[30] graphene hydrogel (0.223 mWh/cm³),^[67] screen-printed graphene (SPG) (~0.2 mWh/cm³),^[68] and

laser-induced porous carbon fiber (0.436 mWh/cm³).^[52] Additionally, the LA-FLAG/CNT MSCs delivered an impressive power density of 7.33 W/cm³, which is comparable to that of electrolytic capacitors and exceeds the power densities of most reported MSCs. This underscores the substantial advancements made with LA-FLAG/CNT MSCs in the field of micro-sized energy storage devices (Table S4). These attributes position the LA-FLAG/CNT MSCs as highly promising candidates for next-generation energy storage solutions, especially in the realm of wearable and flexible electronics.

Conclusions

In conclusion, this study demonstrates the successful fabrication of LA-FLAG/CNT micro-supercapacitors (MSCs) with remarkable

performance, showing their great potential as advanced energy storage devices. By integrating flash lamp annealing (FLA) and laser ablation techniques, we achieved scalable and efficient production of interdigitated graphene/CNT microelectrodes on flexible substrates. This novel approach enabled the fast, millisecond-scale reduction of graphene oxide (GO) and allowed the patterning of numerous graphene/CNT microelectrodes on a single flexible substrate in a short time. The structural and electrochemical analyses revealed that the LA-FLAG/CNT MSCs have significantly enhanced material properties, including increased interlayer spacing, larger specific surface area, and fewer defects. These improvements translated into exceptional electrochemical performance, with an impressive areal capacitance of 26.11 mF/cm^2 and volumetric capacitance of 31.88 F/cm^3 , surpassing many existing carbon-based MSCs. The devices also demonstrated excellent mechanical flexibility, retaining 97% of their capacitance even under extreme bending conditions, further proving their durability for flexible applications.

The scalability and adaptability of LA-FLAG/CNT MSCs were validated by successfully creating series and parallel configurations without additional interconnections, enhancing their operational voltage and capacitance. Additionally, the devices displayed superior volumetric energy density (4.43 mWh/cm^3) and power density (7.33 W/cm^3), as shown in the Ragone plot, making them ideal for high-performance wearable and flexible electronics. In summary, the integration of FLA and laser ablation techniques offers a cost-effective, scalable pathway for producing high-performance MSCs. The excellent electrochemical properties, combined with their mechanical robustness, highlight the potential of LA-FLAG/CNT MSCs for next-generation energy storage systems. Future work will focus on further optimizing the fabrication process and exploring the integration of these MSCs into complex electronic devices, maximizing their full potential.

Methods

Fabrication of LA-FLAG/CNT MSCs

Graphene oxide (GO) was synthesized using a modified Hummer's method.^[69–71] Initially, GO powder was dispersed in water to create a 1.0 wt% dispersion under stirring and sonication. Separately, carbon nanotube (CNT) powder was dispersed in water to achieve 0.3 wt% using a high-pressure homogenizer. The two aqueous dispersions of GO and CNT were then mixed with a predetermined ratio. This GO/CNT aqueous dispersion was then coated onto a flexible substrate using the blade-coating method and dried under ambient condition.

For the synchronous reduction and expansion of GO/CNT composites, intense pulsed light from a xenon (Xe) flash lamp, emitting wavelengths from approximately 200 nm to 1500 nm, was employed. The GO/CNT-coated film was subjected to high-intensity light pulses for tens of microseconds at ambient conditions. A reflector was used to focus the emitted radiation into a sample holder, achieving high photonic energy densities. The GO/CNT film was positioned approximately 10 mm from the flash lamp and exposed to short pulses of high-intensity light. The parameters of

the flash lamp annealing (FLA) process, such as pulse intensity, pulse length, and flashing frequency, were adjusted to control the radiation energy, typically varying the pulse length within specific millisecond ranges and photonic energy from 1 to 10 J/cm^2 .

Subsequently, a 50 nm layer of gold was thermally evaporated onto the FLAG/CNT film at a rate of $\sim 1 \text{ Å/s}$ and a chamber pressure of $5 \times 10^{-7} \text{ Torr}$. The FLAG/CNT composite films were then patterned into comb-like interdigitated electrodes using laser ablation, resulting in planar LA-FLAG/CNT microelectrodes with various geometries and sizes. The LA-FLAG/CNT MSCs were coated with a polymer gel electrolyte of PVA-H₂SO₄. Prior to the electrochemical performance test, the LA-FLAG/CNT MSCs were left under ambient conditions overnight to ensure full penetration and solidification of the electrolyte within the electrodes. The PVA-H₂SO₄ gel electrolyte was prepared as follows: 1 g of PVA ($n \approx 1700$, TCI chemical) was added to 10 ml of H₂O and heated to $\sim 80^\circ\text{C}$ under constant stirring until a clear solution formed. After cooling, 1 ml of sulfuric acid (H₂SO₄, 95–98%, JT Baker) was added, and the solution was stirred thoroughly.

Materials Characterization

The characterization of the samples was performed using scanning electron microscopy (SEM) (FEI, Quanta 450 FEG), X-ray photoelectron spectroscopy (XPS) (Thermo Scientific, K Alpha+), X-ray diffraction (XRD) (PANalytical, X'pert-pro MPD), Brunauer-Emmett-Teller (BET) (Microtrac BEL Corp, BELSORP-max) and Raman spectroscopy (532 nm, XpertRam35Vm Nanobase)

Electrochemical Characterization

Cyclic voltammetry (CV) and galvanostatic charge-discharge (GCD) tests were conducted using a AUTOLAB PGSTAT204 electrochemical workstation (Metrohm) under ambient conditions. The CV tests were performed at scan rates ranging from 10 mV/s to 2 V/s, and the GCD tests were conducted at current densities ranging from 0.1 A/cm^2 to 10 A/cm^2 .

Calculation

Capacitance values were calculated from CV data using the following equation:

$$C_{device} = \frac{1}{\nu(V_f - V_i)} \int_{V_i}^{V_f} I(V) dV \quad (1)$$

where C_{device} is the capacitance, ν is the scan rate (in V/s). V_f and V_i are the potential limits of the CV curve, and $I(V)$ is the voltammetric discharge current (in A).

Capacitance was also calculated based on the GCD curve using the following equation:

$$C_{device} = i / \left(\frac{dV}{dt} \right) \quad (2)$$

where i is applied current (in A) and $\frac{dV}{dt}$ is slope of the discharge curve (in V/s).

Specific capacitances were calculated in term of the area or the volume of the device stack using the formulas:

$$C_{\text{areal}} = \frac{C_{\text{device}}}{A} \quad (3)$$

where C_{areal} (in F/cm^2) and C_{vol} (in F/cm^3) refer to the areal and volumetric capacitance of the device, respectively. A is the total area (in cm^2) and V is the total volume (cm^3) of the device, including interspaces between the electrodes and the entire volume of the electrodes.

The energy density of the devices was calculated using:

$$E_d = \frac{1}{2} \times C_{\text{vol}} \times \frac{(\Delta V)^2}{3,600} \quad (5)$$

where E_d is the energy density (in Wh/cm^3), C_{vol} is the volumetric capacitance, and ΔV is the operating voltage window (in V).

The power density of devices was calculated using:

$$P_d = \frac{E_d}{\Delta t} \times 3,600 \quad (6)$$

where P_d is the power density (in W/cm^3) and Δt is the discharge time (in s).

Acknowledgements

This work was supported by the National Research Foundation of Korea (NRF) grant funded by the Korea government (MSIT) (No. 2022R1 A2 C1093082). This research was supported by the Commercialization Promotion Agency for R&D Outcomes (COMPA) funded by the Ministry of Science and ICT (MSIT) (RS2024-00397698). This work was supported by the Gachon University research fund of 2019 (GCU-2019-0832).

Conflict of Interests

The authors declare no conflict of interest.

Data Availability Statement

The data that support the findings of this study are available from the corresponding author upon reasonable request.

Keywords: Graphene • Flash lamp annealing • Micro-supercapacitors • Supercapacitors • Micro-power sources

- [1] M. Beidaghi, Y. Gogotsi, *Energy & Environmental Sci.* **2014**, *7*(3), 867–884.
- [2] N. A. Kyerematen, T. Brousse, D. Pech, *Nature Nanotechnol.* **2017**, *12*(1), 7–15.
- [3] W. Zhang, Y. Lei, F. Ming, Q. Jiang, P. M. Costa, H. N. Alshareef, *Adv. Energy Mater.* **2018**, *8*(27), 1801840.
- [4] N. Mahmood, C. Zhang, H. Yin, Y. Hou, *J. Mater. Chem. A* **2014**, *2*(1), 15–32.
- [5] B. E. Conway, *Electrochemical supercapacitors: scientific fundamentals and technological applications*, Springer Science & Business Media **2013**.
- [6] Z.-S. Wu, X. Feng, H.-M. Cheng, *National Sci. Rev.* **2014**, *1*(2), 277–292.

- [7] J. J. Yoo, K. Balakrishnan, J. Huang, V. Meunier, B. G. Sumpter, A. Srivastava, M. Conway, A. L. Mohana Reddy, J. Yu, R. Vajtai, *Nano Lett.* **2011**, *11*(4), 1423–1427.
- [8] Z. S. Wu, K. Parvez, X. Feng, K. Müllen, *Nature Comm.* **2013**, *4*(1), 1–8.
- [9] X. Wang, Q. Zhang, *Energy Technol.* **2019**, *7*(11), 1900820.
- [10] L. Wang, X. Bi, S. Yang, *Adv. Mater.* **2016**, *28*(35), 7672–7679.
- [11] J. Qin, J. Gao, X. Shi, J. Chang, Y. Dong, S. Zheng, X. Wang, L. Feng, Z. S. Wu, *Adv. Funct. Mater.* **2020**, *30*(16), 1909756.
- [12] L. Liu, D. Ye, Y. Yu, L. Liu, Y. Wu, *Carbon* **2017**, *111*, 121–127.
- [13] P. Yadav, A. Basu, A. Suryawanshi, O. Game, S. Ogale, *Adv. Mater. Inter.* **2016**, *3*(11), 1600057.
- [14] Y. Lim, J. Yoon, J. Yun, D. Kim, S. Y. Hong, S.-J. Lee, G. Zi, J. S. Ha, *ACS Nano* **2014**, *8*(11), 11639–11650.
- [15] Z. Niu, L. Zhang, L. Liu, B. Zhu, H. Dong, X. Chen, *Adv. Mater.* **2013**, *25*(29), 4035–4042.
- [16] W. W. Liu, Y. Q. Feng, X. B. Yan, J. T. Chen, Q. J. Xue, *Adv. Funct. Mater.* **2013**, *23*(33), 4111–4122.
- [17] W. Liu, C. Lu, X. Wang, R. Y. Tay, B. K. Tay, *ACS Nano* **2015**, *9*(2), 1528–1542.
- [18] S. Wang, Z.-S. Wu, S. Zheng, F. Zhou, C. Sun, H.-M. Cheng, X. Bao, *ACS Nano* **2017**, *11*(4), 4283–4291.
- [19] J. Chmiola, C. Largeot, P.-L. Taberna, P. Simon, Y. Gogotsi, *Science* **2010**, *328*(5977), 480–483.
- [20] L. Wei, N. Nitta, G. Yushin, *ACS Nano* **2013**, *7*(8), 6498–6506.
- [21] W. J. Hyun, E. B. Secor, C. H. Kim, M. C. Hersam, L. F. Francis, C. D. Frisbie, *Adv. Energy Mater.* **2017**, *7*(17), 1700285.
- [22] H. Pang, Y. Zhang, W.-Y. Lai, Z. Hu, W. Huang, *Nano Energy* **2015**, *15*, 303–312.
- [23] K.-H. Choi, J. Yoo, C. K. Lee, S.-Y. Lee, *Energy Environ. Sci.* **2016**, *9*(9), 2812–2821.
- [24] H. Hu, Z. Pei, C. Ye, *Energy Storage Mater.* **2015**, *1*, 82–102.
- [25] Y. G. Zhu, Y. Wang, Y. Shi, J. I. Wong, H. Y. Yang, *Nano Energy* **2014**, *3*, 46–54.
- [26] M. F. El-Kady, R. B. Kaner, *Nature Commun.* **2013**, *4*(1), 1–9.
- [27] Z. Peng, R. Ye, J. A. Mann, D. Zakhidov, Y. Li, P. R. Smalley, J. Lin, J. M. Tour, *ACS Nano* **2015**, *9*(6), 5868–5875.
- [28] J. Lin, Z. Peng, Y. Liu, F. Ruiz-Zepeda, R. Ye, E. L. Samuel, M. J. Yacaman, B. I. Yakobson, J. M. Tour, *Nature Commun.* **2014**, *5*(1), 1–8.
- [29] H.-C. Huang, C.-J. Chung, C.-T. Hsieh, P.-L. Kuo, H. Teng, *Nano Energy* **2016**, *21*, 90–105.
- [30] S. Park, H. Lee, Y.-J. Kim, P. S. Lee, *NPG Asia Mater.* **2018**, *10*(10), 959–969.
- [31] Z.-S. Wu, K. Parvez, X. Feng, K. Müllen, *J. Mater. Chem. A* **2014**, *2*(22), 8288–8293.
- [32] Z.-S. Wu, S. Yang, L. Zhang, J. B. Wagner, X. Feng, K. Müllen, *Energy Storage Mater.* **2015**, *1*, 119–126.
- [33] Z. S. Wu, K. Parvez, A. Winter, H. Vieker, X. Liu, S. Han, A. Turchanin, X. Feng, K. Müllen, *Adv. Mater.* **2014**, *26*(26), 4552–4558.
- [34] Z. Liu, Z. S. Wu, S. Yang, R. Dong, X. Feng, K. Müllen, *Adv. Mater.* **2016**, *28*(11), 2217–2222.
- [35] G. Williams, B. Seger, P. V. Kamat, *ACS Nano* **2008**, *2*(7), 1487–1491.
- [36] Y. L. Zhang, L. Guo, H. Xia, Q. D. Chen, J. Feng, H. B. Sun, *Adv. Opt. Mater.* **2014**, *2*(1), 10–28.
- [37] J. Cai, C. Lv, A. Watanabe, *Nano Energy* **2016**, *30*, 790–800.
- [38] A. Lamberti, M. Serrapède, G. Ferraro, M. Fontana, F. Perrucci, S. Bianco, A. Chiolerio, S. Bocchini, *2D Mater.* **2017**, *4*(3), 035012.
- [39] S. Wang, Y. Yu, R. Li, G. Feng, Z. Wu, G. Compagnini, A. Gulino, Z. Feng, A. Hu, *Electrochimica Acta* **2017**, *241*, 153–161.
- [40] D. Shen, G. Zou, L. Liu, W. Zhao, A. Wu, W. W. Duley, Y. N. Zhou, *ACS Appl. Mater. & Inter.* **2018**, *10*(6), 5404–5412.
- [41] R.-Z. Li, R. Peng, K. D. Kihm, S. Bai, D. Bridges, U. Tumuluri, Z. Wu, T. Zhang, G. Compagnini, Z. Feng, *Energy & Environ. Sci.* **2016**, *9*(4), 1458–1467.
- [42] Y. Wu, Y. Zhang, Y. Liu, P. Cui, S. Chen, Z. Zhang, J. Fu, E. Xie, *ACS Appl. Mater. Inter.* **2020**, *12*(38), 42933–42941.
- [43] M. Khandelwal, C. Van Tran, J. Lee, J. B. In, *Chem. Eng. J.* **2022**, *428*, 131119.
- [44] R. McMahon, M. Smith, K. Seffen, M. Voelskow, W. Anwand, W. Skorupa, *Vacuum* **2007**, *81*(10), 1301–1305.
- [45] L. J. Cote, R. Cruz-Silva, J. Huang, *J. Am. Chem. Society* **2009**, *131*(31), 11027–11032.
- [46] A. Tyagi, Y. Myung, K. M. Tripathi, T. Kim, R. K. Gupta, *Electrochimica Acta* **2020**, *334*, 135590.
- [47] C. Shen, X. Wang, W. Zhang, F. Kang, *J. Power Sources* **2011**, *196*(23), 10465–10471.

- [48] G. Xiong, C. Meng, R. G. Reifenberger, P. P. Irazoqui, T. S. Fisher, *Electroanalysis* **2014**, 26(1), 30–51.
- [49] W. Gao, N. Singh, L. Song, Z. Liu, A. L. M. Reddy, L. Ci, R. Vajtai, Q. Zhang, B. Wei, P. M. Ajayan, *Nature Nanotechnol.* **2011**, 6(8), 496–500.
- [50] J. Lin, C. Zhang, Z. Yan, Y. Zhu, Z. Peng, R. H. Hauge, D. Natelson, J. M. Tour, *Nano Lett.* **2013**, 13(1), 72–78.
- [51] G. Sun, J. An, C. K. Chua, H. Pang, J. Zhang, P. Chen, *Electrochim. Commun.* **2015**, 51, 33–36.
- [52] X. Mu, J. Du, Y. Li, H. Bai, H. Zhao, Z. Wei, B. Huang, Y. Sheng, Z. Zhang, E. Xie, *Carbon* **2019**, 144, 228–234.
- [53] Y. Gao, S. Zheng, H. Fu, J. Ma, X. Xu, L. Guan, H. Wu, Z.-S. Wu, *Carbon* **2020**, 168, 701–709.
- [54] J. Hu, J. Luo, Z. Xu, K. Xie, H. Yu, H. Wang, C. Shen, L.-H. Qi, B. Wei, *Appl. Phys. Rev.* **2021**, 8(1), 011401.
- [55] M. F. El-Kady, V. Strong, S. Dubin, R. B. Kaner, *Science* **2012**, 335(6074), 1326–1330.
- [56] D. Pech, M. Brunet, H. Durou, P. Huang, V. Mochalin, Y. Gogotsi, P.-L. Taberna, P. Simon, *Nature Nanotechnol.* **2010**, 5(9), 651–654.
- [57] D. Aradilla, M. Delaunay, S. Sadki, J.-M. Gérard, G. Bidan, *J Mater. Chem. A* **2015**, 3(38), 19254–19262.
- [58] Y. Ma, M. Wang, N. Kim, J. Suhr, H. Chae, *J Mater. Chem. A* **2015**, 3(43), 21875–21881.
- [59] B. Hsia, J. Marszewski, S. Wang, J. B. In, C. Carraro, D. Poulikakos, C. P. Grigopoulos, R. Maboudian, *Nanotechnology* **2014**, 25(5), 055401.
- [60] D. Yu, K. Goh, H. Wang, L. Wei, W. Jiang, Q. Zhang, L. Dai, Y. Chen, *Nature Nanotechnol.* **2014**, 9(7), 555–562.
- [61] C. Meng, J. Maeng, S. W. John, P. P. Irazoqui, *Adv. Energy Mater.* **2014**, 4(7), 1301269.
- [62] X. Yang, C. Cheng, Y. Wang, L. Qiu, D. Li, *science* **2013**, 341(6145), 534–537.
- [63] Y. Gogotsi, P. Simon, *Science* **2011**, 334(6058), 917–918.
- [64] Y. Wang, Y. Zhang, G. Wang, X. Shi, Y. Qiao, J. Liu, H. Liu, A. Ganesh, L. Li, *Adv. Funct. Mater.* **2020**, 30(16), 1907284.
- [65] Y. Wang, Y. Zhang, J. Liu, G. Wang, F. Pu, A. Ganesh, C. Tang, X. Shi, Y. Qiao, Y. Chen, *Energy Storage Mater.* **2020**, 30, 412–419.
- [66] L. Li, E. B. Secor, K. S. Chen, J. Zhu, X. Liu, T. Z. Gao, J. W. T. Seo, Y. Zhao, M. C. Hersam, *Adv. Energy Mater.* **2016**, 6(20), 1600909.
- [67] Y. Dong, L. Wang, L. Ban, W. Du, X. Feng, P. Chen, F. Xiao, S. Wang, B.-F. Liu, *J Power Sourc.* **2018**, 396, 632–638.
- [68] X. Shi, S. Pei, F. Zhou, W. Ren, H.-M. Cheng, Z.-S. Wu, X. Bao, *Energy & Environ. Sci.* **2019**, 12(5), 1534–1541.
- [69] J. Chen, B. Yao, C. Li, G. Shi, *Carbon* **2013**, 64, 225–229.
- [70] T. Kim, G. Jung, S. Yoo, K. S. Suh, R. S. Ruoff, *ACS Nano* **2013**, 7(8), 6899–6905.
- [71] T. Y. Kim, H. W. Lee, M. Stoller, D. R. Dreyer, C. W. Bielawski, R. S. Ruoff, K. S. Suh, *ACS Nano* **2011**, 5(1), 436–442.

Manuscript received: August 26, 2024

Accepted manuscript online: October 14, 2024

Version of record online: November 9, 2024